Article

Not peer-reviewed version

Improved Energy Storage Density and Efficiency of Nd and Mn Co-Doped Ba0.7Sr0.3TiO3 Ceramic Capacitors via Defect Dipole Engineering

Hyunsu Choi , Srinivas Pattipaka , Yong Hoon Son , Young Min Bae , Jung Hwan Park , Chang Kyu Jeong , Han Eol Lee , Jungho Ryu , Geon-Tae Hwang *

Posted Date: 15 September 2023

doi: 10.20944/preprints202309.1044.v1

Keywords: Ceramic capacitors; Donor-acceptor complex; Defect dipole engineering; Dielectric and ferroelectric properties; Energy storage density and efficiency

Preprints (www.preprints.org) | NOT PEER-REVIEWED | Posted: 15 September 2023 doi:10.20944/preprints202309.1044.v1

Article

Improved Energy Storage Density and Efficiency of Nd and Mn Co-Doped $Ba_{0.7}Sr_{0.3}TiO_3$ Ceramic Capacitors via Defect Dipole Engineering

Hyunsu Choi [1,†], Srinivas Pattipaka [1,†], Yong Hoon Son [1], Young Min Bae [1], Jung Hwan Park [2], Chang Kyu Jeong [3], Han Eol Lee [3], Jungho Ryu [4] and Geon-Tae Hwang [1,*]

[1] Department of Materials Science and Engineering, Pukyong National University, 45, Yongso-ro, Nam-Gu, Busan 48513, Republic of Korea.
[2] Department of Mechanical Engineering (Department of Aeronautics, Mechanical and Electronic Convergence Engineering), Kumoh National Institute of Technology, 61 Daehak-ro, Gumi, Gyeongbuk 39177, Republic of Korea
[3] Division of Advanced Materials Engineering, Jeonbuk National University, Jeonju, Jeonbuk, Republic of Korea
[4] School of Materials Science and Engineering, Yeungnam University, 280 Daehak-ro, Gyeongsan-si, Gyeongsangbuk-do 38541, Republic of Korea
* Correspondence: gthwang@pknu.ac.kr.
† First authors.

Abstract: In this paper, we investigate the structural, microstructural, dielectric, and energy storage properties of Nd and Mn co-doped $Ba_{0.7}Sr_{0.3}TiO_3$ [$(Ba_{0.7}Sr_{0.3})_{1-x}Nd_xTi_{1-y}Mn_yO_3$ (BSNTM) ceramics (x = 0, 0.005, and y = 0, 0.0025, 0.005, and 0.01)] via a defect dipole engineering method. The complex defect dipoles $(Mn_{Ti}^{''} - V_O^{\cdot\cdot})^{\cdot}$ and $(Mn_{Ti}^{''} - V_O^{\cdot\cdot})$ between acceptor ions and oxygen vacancies capture electrons, enhancing the breakdown electric field and energy storage performances. XRD, Raman spectroscopy, and microscopic investigations of BSNTM ceramics revealed the formation of a tetragonal phase, increased oxygen vacancies, and reduced grain size with Mn dopant, respectively. The BSNTM ceramics with x=0.005 and y=0 exhibit a high dielectric constant of 2058 and a dielectric loss of 0.026 at 1 kHz. These values gradually decreased to 1876 and 0.019 for x=0.005 and y=0.01 due to the Mn^{2+} ions at Ti^{4+}-site, which facilitates the formation of oxygen vacancies, and prevents the decrease of Ti^{4+}. In addition, the defect dipoles act as a driving force for depolarization to tailor the domain formation energy and domain wall energy, which provides a high difference between the maximum polarization of P_{max} and remnant polarization of P_r (ΔP=10.39 μC/cm²). Moreover, the complex defect dipoles with optimum oxygen vacancies in BSNTM ceramics can provide not only a high ΔP but also reduce grain size, which together improve the breakdown strength from 60.4 to 110.6 kV/cm, giving rise to a high energy storage density of 0.41 J/cm³ and high efficiency of 84.6% for x=0.005 and y=0.01. These findings demonstrate that defect dipoles engineering is an effective method to enhance the energy storage performance of dielectrics for capacitor applications.

Keywords: ceramic capacitors; donor-acceptor complex; defect dipole engineering; dielectric and ferroelectric properties; energy storage density and efficiency

1. Introduction

Dielectric capacitors are key components of pulsed power applications, and are extensively used in microwave communications, electromagnetic devices, hybrid electric vehicles, and high-frequency inverters [1–4]. Notably, dielectric capacitors display ultrahigh power density, ultrafast charge-discharge rates, excellent fatigue resistance, and thermal stability as compared to batteries [5–7]. However, their energy storage density performance is lower than that of batteries because of their low breakdown strength (BDS), which limits their applications in energy storage devices [8–10]. It is thus necessary to develop new dielectric capacitors with high energy storage density and high energy efficiency to meet the increasing demands for energy storage devices.

The key parameters for energy storage in dielectric capacitors, such as the total energy storage density (W_{tot}), recoverable energy density (W_{rec}), and energy efficiency (η) can be calculated by the following equations [7,8,11]:

$$W_{tot} = \int_0^{P_{max}} E\, dP \tag{1}$$

$$W_{rec} = \int_{P_r}^{P_{max}} E\, dP \tag{2}$$

$$\eta = \frac{W_{rec}}{W_{rec}+W_{loss}} \times 100\% \tag{3}$$

where E is the applied electric field, P is induced polarization, P_{max} is maximum polarization, P_r is remnant polarization, and W_{loss} is hysteresis loss (Figure 1). According to these equations, W_{rec} and η can be improved by increasing the difference between P_{max} and P_r ($\Delta P = P_{max} - P_r$) and the BDS/breakdown electric field (E_{BD}), which means that energy storage mostly depends on the ΔP and E_{BD} parameters, hence a larger E_{BD} is the cause of high energy storage density. Normally, high dielectric constant materials with a large P_{max} display high dielectric loss, which leads to low BDS and W_{rec} [12]. Researchers have sought to enhance the BDS by modifying extrinsic properties, such as reducing the thickness of dielectric capacitors [13,14], porosity [15,16], grain size [17,18], and adopting a core-shell structure [19,20]. They have also modified intrinsic properties, including enhancing the bandgap energy [8,21], tailoring electrical homogeneity, and reducing electrical conductivity [22].

In recent years, lead-free dielectric capacitors have received significant attention, and a great deal of research has been carried out to enhance the energy storage properties due to lead toxicity and environmental issues. Lead-free dielectrics, such as $BaTiO_3$ (BT) [23–25], $Bi_{0.5}Na_{0.5}TiO_3$ (BNT) [26–30], $BiFeO_3$ (BFO) [22,31,32], and $K_{0.5}Na_{0.5}NbO_3$ (KNN) [33,34]-based materials/composites afford improved energy storage performance and energy efficiency for energy storage applications. In particular, the BT-based ceramics are potential candidates and are widely used for capacitor applications due to their high polarization, high dielectric constant, and low Curie temperature (T_C) [35,36]. Few oxide materials (Al_2O_3, SiO_2, and MgO) are used as additives to improve the BDS and energy storage properties of BT-based ceramics [37–39]. Rafik *et al.* [40] reported Sr substitution at the A-site of BT ($Ba_{0.7}Sr_{0.3}TiO_3$) ceramics and improved dielectric properties. However, oxygen vacancies and conduction electrons can occur during the sintering process of BT-based ceramics at high temperatures, resulting in a high dielectric loss [41].

Aliovalent doping is an effective method for tailoring the electrical properties of oxide materials. The use of donor dopants, such as La and Nd, is an effective approach to compensate for the formation of oxygen vacancies for improving the dielectric properties of BT ceramics. Morison and Shaikh *et al.* [42,43] reported La and Nd doped BT ceramics with a high dielectric constant of 25,000 and 13,000 at T_C, respectively. On the other hand, acceptor (Mn^{2+} at Ti^{4+}-site) doping in BT ceramics promotes the formation of oxygen vacancies and minimizes the decrease of Ti^{4+} during the sintering process in low oxygen atmospheres. Therefore, Mn-doped BT decreases dielectric loss [44–46]. Recently, Yueshun *et al.* [47] demonstrated defect dipoles by oxygen vacancies in acceptor doped (specifically Fe) $Sr_2Bi_4Ti_{(5-x)}Fe_xO_{18}$ (x=0.04–0.12) and enhanced E_{BD} and energy storage properties.

In this paper, we present a defect dipoles engineering method to improve the breakdown strength and energy storage performance by co-doping of Nd and Mn in $Ba_{0.7}Sr_{0.3}TiO_3$ (BST) ceramics that have been prepared via the traditional solid-stated reaction method. The Nd-doped BST [$(Ba_{0.7}Sr_{0.3})_{1-x}Nd_xTiO_3$, BSNT] ceramics can compensate for the formation of oxygen vacancies, improving the dielectric constant of BSNT ceramics. In contrast, Mn-doped BSNT ceramics [$(Ba_{0.7}Sr_{0.3})_{1-x}Nd_xTi_{1-y}Mn_yO_3$, BSNTM] facilitate the formation of oxygen vacancies, prevent the decrease of Ti^{4+}, and yield low dielectric loss. Therefore, simultaneously, a high dielectric constant and low dielectric loss can be expected with Nd and Mn co-dopants in BST. Moreover, the complex defect dipoles with uniform and small-grained microstructure provide a high difference between P_{max} and P_r (ΔP of 10.39 μC/cm^2) and show improved breakdown strength of 110.6 kV/cm with Nd and Mn, which results in a high energy storage density of 0.41 J/cm^3 and high efficiency of 84.6% in BSNTM ceramics, as schematically shown in Figure 1.

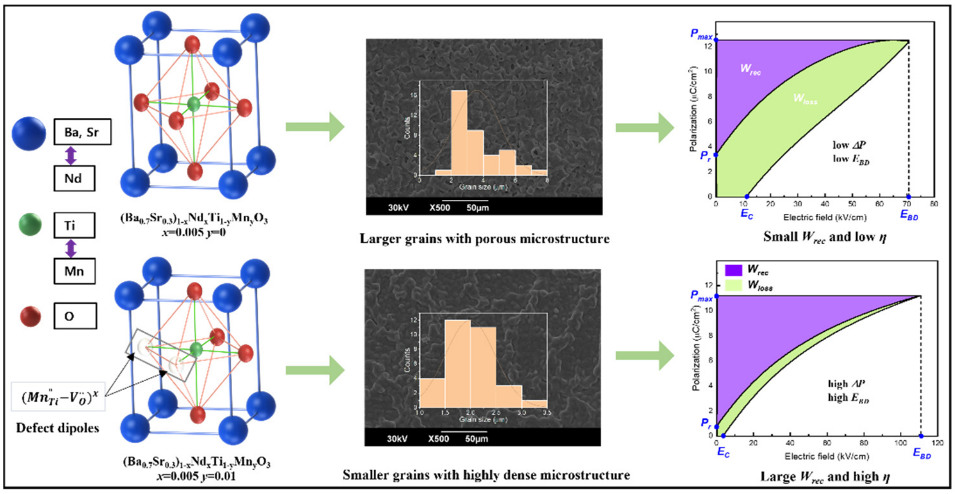

Figure 1. Schematic illustration for energy storage performance of Nd and Mn co-doped BST ceramics. Defect dipoles $(Mn_{Ti}^{''}-V_O^{\cdot\cdot})^x$ between acceptor ions and oxygen vacancies capture electrons, reduce grain size, and provide a high difference between P_{max} and P_r, which improve the breakdown electric field with Mn, resulting in a high energy storage density and high energy efficiency in BSNTM ceramics.

2. Materials and Methods

$(Ba_{0.7}Sr_{0.3})_{1-x}Nd_xTi_{1-y}Mn_yO_3$ (BSNTM) (x=0, 0.005, and y=0, 0.0025, 0.005, and 0.01) lead-free ceramics were synthesized by the traditional solid-state reaction method. The raw materials $BaCO_3$ (Sigma-Aldrich, 99%), $SrCO_3$ (Sigma-Aldrich, 98%), Nd_2O_3 (Sigma-Aldrich, 99.9%), TiO_2, (Sigma-Aldrich, 99%), and MnO_2 (Sigma-Aldrich, 99%) were weighed in stoichiometric proportions and ball-milled for 24h. After drying the slurry, the BSNTM powder was calcined at 1150 °C for 3h to obtain the phase of BSNTM. Further, 3 wt.% of Li_2CO_3 (Junsei, 99%) powder was added to this calcined powder as a sintering aid, and the powder was again ball milled for 12h to reduce the sintering temperature and increase its bulk density. Subsequently, 5 wt.% of polyvinyl alcohol (Sigma-Aldrich, 99%) was added and the powder was pressed into pellets with dimensions of 10 mm in diameter and 0.5 mm in thickness at a pressure of 10 MPa followed by sintering at 1050 °C for 2h. Finally, silver paste (ELCOAT, Electroconductives) was applied on both surfaces of the prepared pellets of BSNTM to carry out electrical characterizations.

The crystal structure of the BSNTM samples was tested using an X-ray diffractometer (Rigaku, TTRAX III 18 kW) and Raman spectroscopy (JOBIN YVON, LABRAM HR800). A field emission scanning electron microscope (FESEM, JEOL, JSM-7610F) was used to examine the microstructural properties. Room temperature (RT) dielectric constant and dielectric loss were measured in the frequency range of 100 Hz – 100 kHz by an impedance analyzer (Hewlett Packard, 4294A). Ferroelectric properties (*P*-*E* loops) were measured using a ferroelectric tester (Aix ACT, TF Analyzer 2000).

3. Results and discussion

3.1. Phase formation and crystal structure

Figure 2(a) shows the X-ray diffraction (XRD) patterns of BSNTM ceramics for x=0, and 0.005 and y=0, 0.0025, 0.005 and 0.01 in the 2θ range of 20–90°. All the samples exhibited a single phase with a tetragonal crystal structure (P4mm space group), demonstrating that Nd and Mn are incorporated into the BST system without any secondary phase. At RT, the $Ba_{1-x}Sr_xTiO_3$ ceramics exhibit a tetragonal crystal structure at x=0.3, as reported by Rafik *et al.*[40]. However, there is no evidence for peak splitting/changes in the crystal structure with the substitution of Nd and Mn into BST ceramics. In Figure 2(b), it can be seen that the position of the predominant (101) diffraction peak shifted towards higher angles with Nd for x=0.005 and y=0, and further, it shifted back to lower angles with Mn into BST for x=0.005 and y=0.0025–0.01. The shift towards lower and higher angles in the diffraction peak demonstrates an increase and decrease in the lattice parameters due to incorporating Nd and Mn in the BST system, respectively. For x=0.005 and y=0, the Nd^{3+} (1.27 Å) ions can be occupied at the A-site of Ba^{2+} (1.61 Å) and Sr^{2+} (1.12 Å), whereas Mn^{2+} (0.66 Å) ions occupied at the B-site of Ti^{4+} (0.60 Å) site of the BST system for x=0.005 and y=0.0025–0.01 due to their mismatch of ionic radii and valences [40,48]. This indicates that the rise in oxygen vacancies accounts for the increase in lattice volume. To maintain charge balance, acceptor doping of Mn^{3+} and Mn^{2+} occupying at Ti^{4+} leads to a loss of positive charge and releasing lattice oxygen in the form of O_2 [49]. The lack of lattice oxygen makes it challenging for the surrounding cations' positive charges to be neutralized, which causes the radii of the oxygen vacancies to increase as a result of higher Coulomb repulsion forces [50]. In addition, the lattice oxygen radius (140 pm) is substantially smaller than the oxygen vacancy radius (151.5 pm). As a result, the lattice increases because the oxygen vacancies gradually rise with Mn [51].

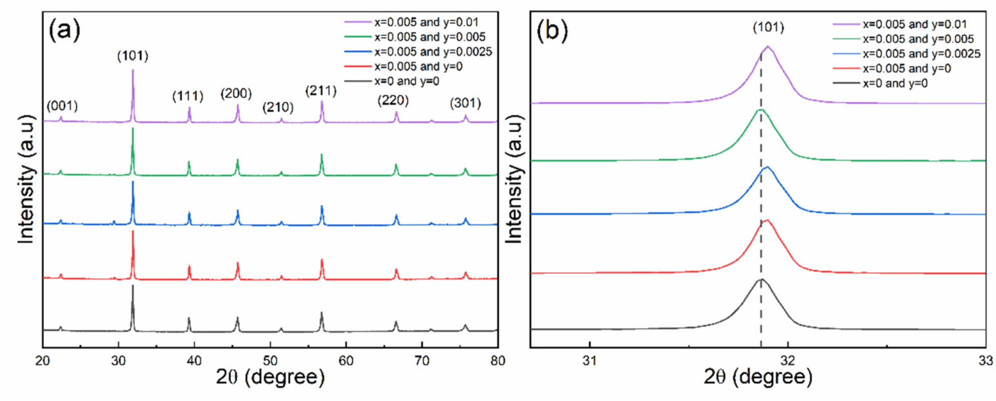

Figure 2. (a) XRD patterns of $(Ba_{0.7}Sr_{0.3})_{1-x}Nd_xTi_{1-y}Mn_yO_3$ ceramics for x=0, and 0.005, and y=0, 0.0025, 0.005, and 0.01. (b) Shift in (101) diffraction peak in the 2θ range from 30.7 – 33°.

Raman spectra of BSNTM ceramics in the range of 100–1000 cm^{-1}, are shown in Figure 3. The Raman bands of all samples indicate the tetragonal phase of the perovskite structure in BST ceramics, is similar to BST-based reports [40,48]. The spectral parameters of the Raman modes, such as the Raman shift of the central position of each peak and corresponding full width at half maxima (FWHM), are calculated by fitting the Gaussian function. A total of nine Raman active modes were observed. The modes appeared around 135 and 168 cm^{-1} associated with the vibration of A-site cations (A-O), 213, 271, 351 cm^{-1} related to the vibrations of B-O, 510, 539, 565 cm^{-1} related to the vibrations of BO_6, and 740 cm^{-1} corresponds to the A_1 + E (LO) overlapping modes [40]. The mode at 135 cm^{-1} is slightly shifted to a higher wavenumber of 138 cm^{-1} with Nd substitution for x=0.005 and y=0. This is caused by *A*-site disorder, which is attributed to the incorporation of Nd^{3+} at Ba^{2+} and Sr^{2+} ions. The modes around 271 and 539 cm^{-1} shifted towards a lower wavenumber with increasing Mn concentration from x=0.005 and y=0.0025 to 0.01. This is due to an increase in the *B*-site disorder in the BSNTM related to the creation of lattice tensile stress because of lattice expansion [52]. These results demonstrate that the influence of oxygen vacancies at B-site ions is substantially greater than at the A-site because the coordination number of oxygens at the A-site is 12, whereas that at the B-site is 6 in the perovskite structure. These results are well supported by XRD, dielectric, and ferroelectric properties.

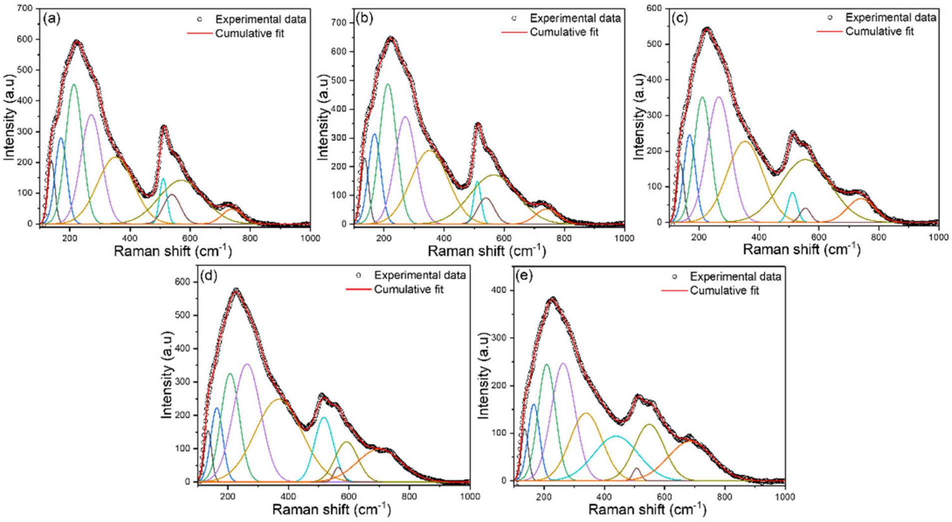

Figure 3. Raman spectra of $(Ba_{0.7}Sr_{0.3})_{1-x}Nd_xTi_{1-y}Mn_yO_3$ ceramics for (a) x=0 and y=0, (b) x=0.005 and y=0, (c) x=0.005 and y=0.0025 (d) x=0.005 and y=0.005, and (e) x=0.005 and y=0.01.

3.2. Microstructural properties

FESEM images of the BSNTM ceramics are shown in Figure 4. The x=0.005 and y=0.01 sample shows a uniform microstructure and has a more compact grain size distribution compared to pure BST and other samples of BSNTM (x=0.005 and y<0.01). The density of BSNTM ceramics was estimated by the Archimedes principle to confirm a dense and uniform microstructure. The estimated relative density was found to be in the range of 91% to 98% of the theocratical density, thus verifying that all the samples have a highly dense and uniform microstructure. The average grain size of the BSNTM (x=0 and y=0) was found to be 3.59 µm and is reduced to 1.99 µm with substitution of Nd and Mn co-dopants in BSNTM for x=0.005 and y=0.01. The reduction in grain size with a uniform microstructure is due to the formation of oxygen vacancies caused by Mn^{2+} occupying Ti^{4+}. Soo and Qiaoli *et al.* [48,53] reported that the Sm and Yb and Nd and Mn co-doped BT ceramics with donor/donor-acceptor defect complexes by charge-compensation/oxygen vacancy exhibited uniform and small-grained microstructure. The smaller grains with a uniform and dense microstructure can resist higher voltages, which results in high BDS and enhanced energy storage properties [54,55].

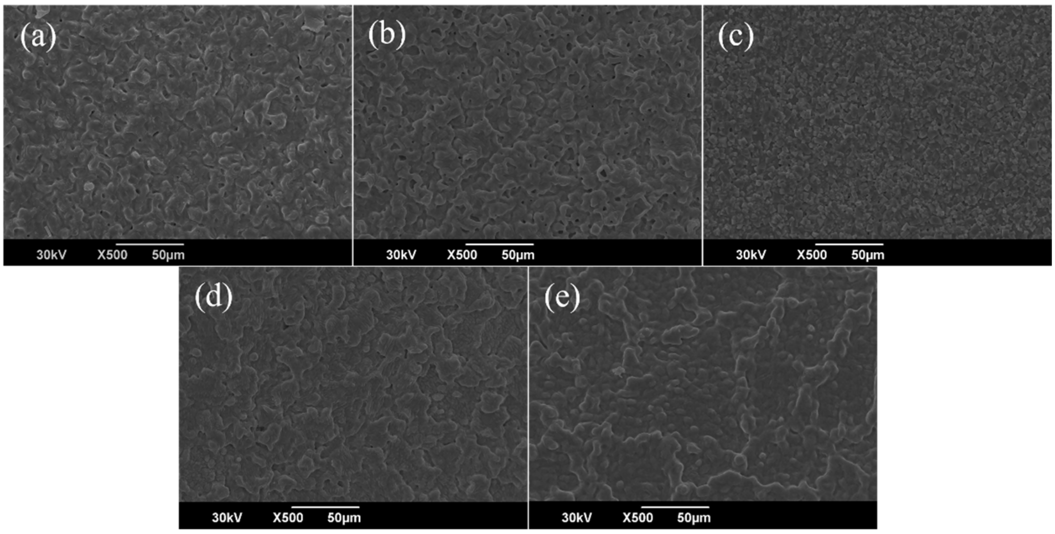

Figure 4. FESEM images of $(Ba_{0.7}Sr_{0.3})_{1-x}Nd_xTi_{1-y}Mn_yO_3$ ceramics for (a) x=0 and y=0, (b) x=0.005 and y=0, (c) x=0.005 and y=0.0025 (d) x=0.005 and y=0.005, and (e) x=0.005 and y=0.01.

3.3. Dielectric properties

The dielectric constant (ε_r) and the dielectric loss ($tan\delta$) of BSNTM ceramic capacitors measured as a function frequency at RT from 100 Hz to 100 kHz are shown in Figure 5. Pure BST (x=0 and y=0) exhibited a ε_r of 1868 and $tan\delta$ of 0.0218 at 1 kHz, which are improved to 2058 and 0.0266 with Nd substitution for x=0.005 and y=0. Further, these values gradually decreased to 1876 and 0.0191 with Mn substitution into BSNTM for x=0.005 and y=0.01. The Nd and Mn co-dopants in the BST matrix favor the formation of donor-acceptor complexes. The Nd^{3+} ions in the BST system can compensate for the formation of oxygen vacancies, leading to enhancement of the dielectric constant of BSNT ceramics. On the other hand, Mn^{2+} ions in the BSNT system facilitate the formation of oxygen vacancies, prevent the decrease of Ti^{4+}, and yield low dielectric loss. Therefore, a high dielectric constant and low dielectric loss can be achieved simultaneously with Nd and Mn co-dopants in BST [48].

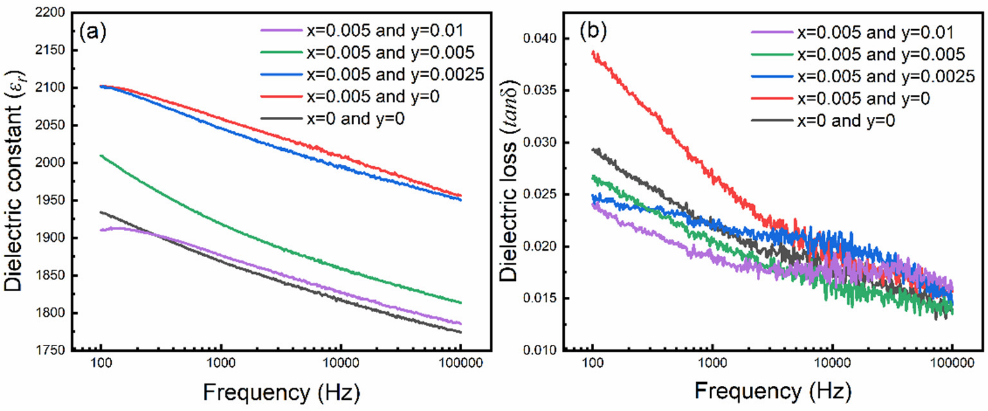

Figure 5. (a) Dielectric constant and (b) dielectric loss as a function of the frequency of $(Ba_{0.7}Sr_{0.3})_{1-x}Nd_xTi_{1-y}Mn_yO_3$ ceramics.

3.4. P-E loops and energy storage performance

P-E loops of BSNTM ceramics measured at RT under different electric fields at a frequency of 10 Hz are shown in Figure 6. The ferroelectric BSNTM (x=0.005 and y=0) ceramics displayed a large maximum polarization P_{max} of 12.5 μC/cm², small remnant polarization P_r of 3.35 μC/cm² (i.e., ΔP=9.15 μC/cm²), and a high coercive field E_c of 11.2 kV/cm. The P_{max}, P_r, and E_c values gradually reduced and increased ΔP from 9.15 to 10.39 μC/cm² and the breakdown electric field E_{BD} from 60.4 to 110.6 kV/cm from x=0.005 and y=0 to x=0.005 and y=0.01, as can be seen in Table 1. The BSNTM sample for x=0.005 and y=0.01 (Figure 6e) exhibits a slim saturated *P-E* loop, and the improved E_{BD} is attributed to the decrease in grain size and defect dipoles generated with the incorporation of Mn at the Ti-site of the BST host lattice; this can be understood by Kroger-Vink notation as follows [47,56].

$$Mn_2O_3 \xrightarrow{(2TiO_2)} 2Mn'_{Ti} + 3O_o + V_o^{\cdot\cdot} \qquad (4)$$

$$MnO \xrightarrow{(TiO_2)} Mn''_{Ti} + O_o + V_o^{\cdot\cdot} \qquad (5)$$

It shows that the oxygen vacancies are generated by Mn^{3+} and Mn^{2+} replacing Ti^{4+} at the B-site. In Eq. 4 and 5, $2Ti^{4+}$ needs four lattice oxygen O_o to charge neutrality, whereas $2Mn^{3+}$ requires $3O_o$. When $2Mn^{3+}$ substitutes at $2Ti^{4+}$, $1O_o$ is released as ½ O_2, generating oxygen vacancies $V_o^{\cdot\cdot}$ with two positive charges. Thus, Mn^{2+} replaces Ti^{4+} (Eq. 5) [47].

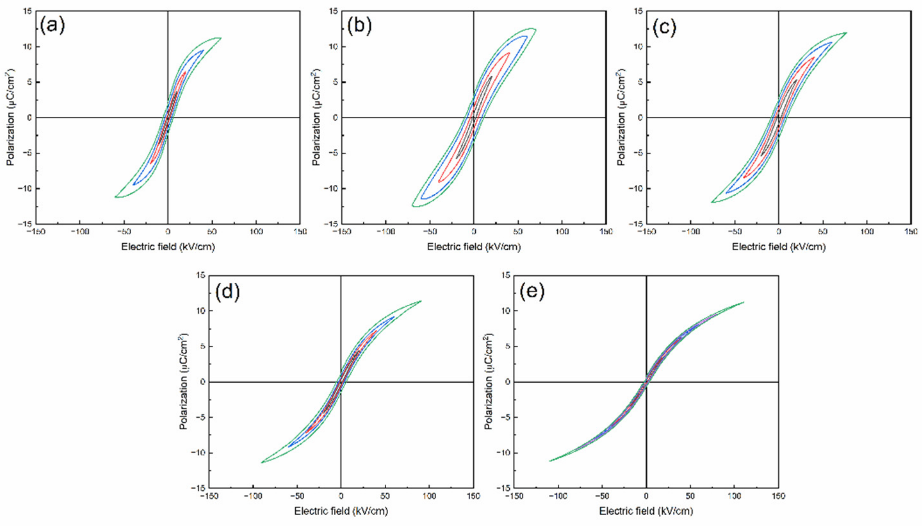

Figure 6. RT Bipolar *P-E* loops of $(Ba_{0.7}Sr_{0.3})_{1-x}Nd_xTi_{1-y}Mn_yO_3$ ceramics measured under different electric fields at 10 Hz for (a) x=0 and y=0, (b) x=0.005 and y=0, (c) x=0.005 and y=0.0025 (d) x=0.005 and y=0.005, and (e) x=0.005 and y=0.01.

Table 1. Ferroelectric and energy storage parameters of BSNTM ceramics.

Composition	**P_r** **C/cm^2)**	**P_{max}** **(μC/cm^2)**	**$\Delta P=P_{max}$-** **P_r**	**E_c** **(kV/cm)**	**E_{BD}** **(kV/cm)**	**W_{rec}** **(J/cm^3)**	**η** **(%)**
x = 0 and y=0	2.22	11.2	8.98	5.94	60.4	0.15	48.5
x = 0.005 and y=0	3.35	12.5	9.15	11.2	70.6	0.19	38.8
x = 0.005 and y=0.0025	2.87	11.9	9.03	9.34	76.6	0.22	48.9
x = 0.005 and y=0.005	1.57	11.4	9.83	5.45	90.5	0.3	69.4
x = 0.005 and y=0.01	0.81	11.2	10.39	3.09	110.6	0.41	84.6

The W_{rec} and η values of BSNTM ceramic capacitors were derived from *P-E* loops by equations (2) and (3), shown in Table 1. The W_{rec} and η values gradually increased with increasing Mn concentration, and the sample with x = 0.005 and y=0.01 exhibits a high energy density of 0.41 J/cm^3 at E_{BD} of 110.6 kV/cm and high energy efficiency of 84.6%, as shown in Figure 7e. The enhancement in the energy storage properties is realized by defect dipole engineering by co-doping of Nd and Mn in BST (mostly governed by Mn). $(Mn_{Ti}'' - V_O^{\cdot\cdot})^{\cdot}$ and $(Mn_{Ti}'' - V_O^{\cdot\cdot})$ defect dipoles between acceptor ions and oxygen vacancies can capture electrons and improve the BDS. In addition, the defect dipoles act as a driving force for depolarization making it possible to design domain formation energy and domain wall energy, which provides a high difference between P_{max} and P_r (ΔP=10.39 μC/cm^2) [47]. Moreover, the complex defect dipoles with optimum oxygen vacancies can provide not only a high ΔP but also reduce the grain size, which together improves the breakdown strength with Mn and leads to high energy storage density and high energy efficiency in BSNTM ceramics. It is well-known that ΔP and E_{BD} are key factors for energy storage performance; i.e., higher ΔP and E_{BD} account for a huge energy storage density and efficiency [57].

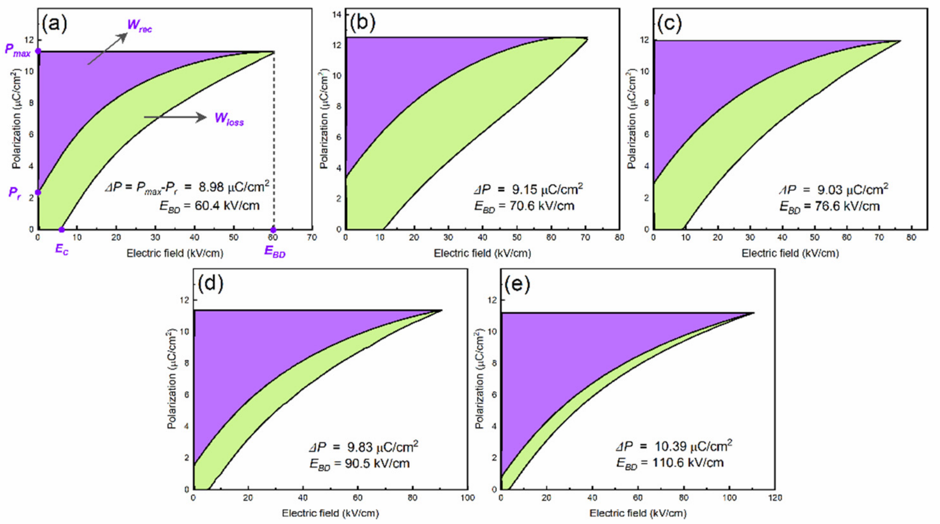

Figure 7. RT unipolar *P-E* loops of $(Ba_{0.7}Sr_{0.3})_{1-x}Nd_xTi_{1-y}Mn_yO_3$ ceramics measured at 10 Hz for (a) x=0 and y=0, (b) x=0.005 and y=0, (c) x=0.005 and y=0.0025 (d) x=0.005 and y=0.005, and (e) x=0.005 and y=0.01.

4. Conclusions

In summary, we demonstrated a defect dipole engineering method to improve the breakdown strength and energy storage properties by co-doping of Nd and Mn in BST ceramics, which are fabricated by a traditional solid-stated reaction method. XRD patterns and Raman spectra of all samples confirmed a single-phase of perovskite structure with a tetragonal phase. FESEM images of BSNTM ceramics exhibit a uniform and dense microstructure, whereas the average grain size reduces with increasing Mn concentration. In addition, the dielectric properties were decreased with Mn due to the formation of oxygen vacancies. Moreover, the complex defect dipoles with smaller grain size and lower dielectric loss provide a high difference between P_{max} and P_r and improve the breakdown strength with Mn, leading to high energy density and efficiency in BSNTM ceramics. These features suggest that defect dipole engineering is an effective approach to enhance the energy storage performance for pulsed-power capacitor applications.

Author Contributions: Measurement, data curation, investigation, and visualization, H. C.; Formal analysis, writing—original draft preparation, review and editing, S.P.; data curation, investigation, Y. H. S.; data curation, investigation, Y. M. B.; visualization, writing-review and editing, J. H. P.; investigation, writing-review and editing, C. K. J.; validation, writing-review and editing, H. E. L.; conceptualization, validation, project administration, supervision, writing-review and editing, J. R.; conceptualization, validation, project administration, supervision, writing-review and editing, G. H. All authors have read and agreed to the published version of the manuscript.

Funding: The work at PKNU was supported by the National Research Foundation of Korea (NRF-2022R1A2C4001497) grant funded by the Ministry of Science and ICT (MSIT). The work conducted at YU was supported by the National Research Foundation of Korea (NRF) grant funded by the Korean government (MSIT) (No. 2023R1A2C2005864).

Institutional Review Board Statement: Not applicable.

Informed Consent Statement: Not applicable.

Data Availability Statement: Not applicable.

Conflicts of Interest: The authors declare no conflict of interest.

References

1. Pan, H.; Li, F.; Liu, Y.; Zhang, Q.; Wang, M.; Lan, S.; Zheng, Y.; Ma, J.; Gu, L.; Shen, Y.; et al. Ultrahigh–Energy Density Lead-Free Dielectric Films via Polymorphic Nanodomain Design. *Science (1979)* **2019**, *365*, 578–582. https://doi.org/10.1126/science.aaw8109.
2. Yao, F.-Z.; Yuan, Q.; Wang, Q.; Wang, H. Multiscale Structural Engineering of Dielectric Ceramics for Energy Storage Applications: From Bulk to Thin Films. *Nanoscale* **2020**, *12*, 17165–17184. https://doi.org/10.1039/D0NR04479B.
3. Li, Q.; Yao, F.-Z.; Liu, Y.; Zhang, G.; Wang, H.; Wang, Q. High-Temperature Dielectric Materials for Electrical Energy Storage. *Annu Rev Mater Res* **2018**, *48*, 219–243. https://doi.org/10.1146/annurev-matsci-070317-124435.
4. Zhao, P.; Cai, Z.; Chen, L.; Wu, L.; Huan, Y.; Guo, L.; Li, L.; Wang, H.; Wang, X. Ultra-High Energy Storage Performance in Lead-Free Multilayer Ceramic Capacitors *via* a Multiscale Optimization Strategy. *Energy Environ Sci* **2020**, *13*, 4882–4890. https://doi.org/10.1039/D0EE03094E.
5. Kumar, N.; Ionin, A.; Ansell, T.; Kwon, S.; Hackenberger, W.; Cann, D. Multilayer Ceramic Capacitors Based on Relaxor BaTiO3-Bi(Zn1/2Ti1/2)O3 for Temperature Stable and High Energy Density Capacitor Applications. *Appl Phys Lett* **2015**, *106*, 252901. https://doi.org/10.1063/1.4922947.
6. Li, J.; Li, F.; Xu, Z.; Zhang, S. Multilayer Lead-Free Ceramic Capacitors with Ultrahigh Energy Density and Efficiency. *Advanced Materials* **2018**, *30*, 1802155. https://doi.org/10.1002/adma.201802155.
7. Zhu, L.-F.; Zhao, L.; Yan, Y.; Leng, H.; Li, X.; Cheng, L.-Q.; Xiong, X.; Priya, S. Composition and Strain Engineered AgNbO$_3$ -Based Multilayer Capacitors for Ultra-High Energy Storage Capacity. *J Mater Chem A Mater* **2021**, *9*, 9655–9664. https://doi.org/10.1039/D1TA00973G.
8. Cao, W.; Lin, R.; Chen, P.; Li, F.; Ge, B.; Song, D.; Zhang, J.; Cheng, Z.; Wang, C. Phase and Band Structure Engineering via Linear Additive in NBT-ST for Excellent Energy Storage Performance with Superior Thermal Stability. *ACS Appl Mater Interfaces* **2022**, *14*, 54051–54062. https://doi.org/10.1021/acsami.2c17170.
9. Zhao, L.; Liu, Q.; Gao, J.; Zhang, S.; Li, J. Lead-Free Antiferroelectric Silver Niobate Tantalate with High Energy Storage Performance. *Advanced Materials* **2017**, *29*, 1701824. https://doi.org/10.1002/adma.201701824.
10. Zheng, T.; Yu, Y.; Lei, H.; Li, F.; Zhang, S.; Zhu, J.; Wu, J. Compositionally Graded KNN-Based Multilayer Composite with Excellent Piezoelectric Temperature Stability. *Advanced Materials* **2022**, *34*, 2109175. https://doi.org/10.1002/adma.202109175.
11. Hu, Q.; Tian, Y.; Zhu, Q.; Bian, J.; Jin, L.; Du, H.; Alikin, D.O.; Shur, V.Y.; Feng, Y.; Xu, Z.; et al. Achieve Ultrahigh Energy Storage Performance in BaTiO3–Bi(Mg1/2Ti1/2)O3 Relaxor Ferroelectric Ceramics via Nano-Scale Polarization Mismatch and Reconstruction. *Nano Energy* **2020**, *67*, 104264. https://doi.org/10.1016/j.nanoen.2019.104264.
12. Qi, H.; Zuo, R. Linear-like Lead-Free Relaxor Antiferroelectric (Bi$_{0.5}$ Na$_{0.5}$)TiO$_3$ –NaNbO$_3$ with Giant Energy-Storage Density/Efficiency and Super Stability against Temperature and Frequency. *J Mater Chem A Mater* **2019**, *7*, 3971–3978. https://doi.org/10.1039/C8TA12232F.
13. Wang, D.; Fan, Z.; Zhou, D.; Khesro, A.; Murakami, S.; Feteira, A.; Zhao, Q.; Tan, X.; Reaney, I.M. Bismuth Ferrite-Based Lead-Free Ceramics and Multilayers with High Recoverable Energy Density. *J Mater Chem A Mater* **2018**, *6*, 4133–4144. https://doi.org/10.1039/C7TA09857J.
14. Zhao, P.; Wang, H.; Wu, L.; Chen, L.; Cai, Z.; Li, L.; Wang, X. High-Performance Relaxor Ferroelectric Materials for Energy Storage Applications. *Adv Energy Mater* **2019**, *9*, 1803048. https://doi.org/10.1002/aenm.201803048.
15. Inam, F.; Yan, H.; Jayaseelan, D.D.; Peijs, T.; Reece, M.J. Electrically Conductive Alumina–Carbon Nanocomposites Prepared by Spark Plasma Sintering. *J Eur Ceram Soc* **2010**, *30*, 153–157. https://doi.org/10.1016/j.jeurceramsoc.2009.05.045.
16. Lu, D.-Y.; Yin, S.; Cui, S.-Z. A Fine-Grained and Low-Loss X8R (Ba1–Dy) (Ti1–/2Ca/2)O3 Ceramic. *J Alloys Compd* **2018**, *762*, 282–288. https://doi.org/10.1016/j.jallcom.2018.05.171.
17. Song, Z.; Liu, H.; Zhang, S.; Wang, Z.; Shi, Y.; Hao, H.; Cao, M.; Yao, Z.; Yu, Z. Effect of Grain Size on the Energy Storage Properties of (Ba0.4Sr0.6)TiO3 Paraelectric Ceramics. *J Eur Ceram Soc* **2014**, *34*, 1209–1217. https://doi.org/10.1016/j.jeurceramsoc.2013.11.039.
18. Lee, H.Y.; Cho, K.H.; Nam, H.-D. Grain Size and Temperature Dependence of Electrical Breakdown in BaTiO$_3$ Ceramic. *Ferroelectrics* **2006**, *334*, 165–169. https://doi.org/10.1080/00150190600694415.
19. Su, X.; Riggs, B.C.; Tomozawa, M.; Nelson, J.K.; Chrisey, D.B. Preparation of BaTiO$_3$ /Low Melting Glass Core–Shell Nanoparticles for Energy Storage Capacitor Applications. *J. Mater. Chem. A* **2014**, *2*, 18087–18096. https://doi.org/10.1039/C4TA04282D.
20. Meng, L.; Zheng, L.; Cheng, L.; Li, G.; Huang, L.; Gu, Y.; Zhang, F. Synthesis of Novel Core-Shell Nanocomposites for Fabricating High Breakdown Voltage ZnO Varistors. *J Mater Chem* **2011**, *21*, 11418. https://doi.org/10.1039/c1jm10807g.
21. Shi, L.N.; Ren, Z.H.; Jain, A.; Jin, R.H.; Jiang, S.S.; Zhou, H.Z.; Chen, F.G.; Wang, Y.G. Enhanced Energy Storage Performance Achieved in Na0.5Bi0.5TiO3–Sr0.7Bi0.2TiO3 Ceramics via Domain Structure and Bandgap Width Tuning. *Ceram Int* **2023**, *49*, 12822–12831. https://doi.org/10.1016/j.ceramint.2022.12.149.

22. Wang, G.; Li, J.; Zhang, X.; Fan, Z.; Yang, F.; Feteira, A.; Zhou, D.; Sinclair, D.C.; Ma, T.; Tan, X.; et al. Ultrahigh Energy Storage Density Lead-Free Multilayers by Controlled Electrical Homogeneity. *Energy Environ Sci* **2019**, *12*, 582–588. https://doi.org/10.1039/C8EE03287D.
23. Yuan, Q.; Li, G.; Yao, F.-Z.; Cheng, S.-D.; Wang, Y.; Ma, R.; Mi, S.-B.; Gu, M.; Wang, K.; Li, J.-F.; et al. Simultaneously Achieved Temperature-Insensitive High Energy Density and Efficiency in Domain Engineered BaTiO3-Bi(Mg0.5Zr0.5)O3 Lead-Free Relaxor Ferroelectrics. *Nano Energy* **2018**, *52*, 203–210. https://doi.org/10.1016/j.nanoen.2018.07.055.
24. Zhao, P.; Wang, H.; Wu, L.; Chen, L.; Cai, Z.; Li, L.; Wang, X. High-Performance Relaxor Ferroelectric Materials for Energy Storage Applications. *Adv Energy Mater* **2019**, *9*, 1803048. https://doi.org/10.1002/aenm.201803048.
25. Asbani, B.; Gagou, Y.; Ben Moumen, S.; Dellis, J.-L.; Lahmar, A.; Amjoud, M.; Mezzane, D.; El Marssi, M.; Rozic, B.; Kutnjak, Z. Large Electrocaloric Responsivity and Energy Storage Response in the Lead-Free Ba(GexTi1−x)O3 Ceramics. *Materials* **2022**, *15*, 5227. https://doi.org/10.3390/ma15155227.
26. Yin, J.; Zhang, Y.; Lv, X.; Wu, J. Ultrahigh Energy-Storage Potential under Low Electric Field in Bismuth Sodium Titanate-Based Perovskite Ferroelectrics. *J Mater Chem A Mater* **2018**, *6*, 9823–9832. https://doi.org/10.1039/C8TA00474A.
27. Qi, H.; Zuo, R. Linear-like Lead-Free Relaxor Antiferroelectric (Bi$_{0.5}$Na$_{0.5}$)TiO$_3$–NaNbO$_3$ with Giant Energy-Storage Density/Efficiency and Super Stability against Temperature and Frequency. *J Mater Chem A Mater* **2019**, *7*, 3971–3978. https://doi.org/10.1039/C8TA12232F.
28. Lu, Y.; Zhang, H.; Yang, H.; Fan, P.; Samart, C.; Takesue, N.; Tan, H. SPS-Prepared High-Entropy (Bi0.2Na0.2Sr0.2Ba0.2Ca0.2)TiO3 Lead-Free Relaxor-Ferroelectric Ceramics with High Energy Storage Density. *Crystals (Basel)* **2023**, *13*, 445. https://doi.org/10.3390/cryst13030445.
29. Jiang, Y.; Niu, X.; Liang, W.; Jian, X.; Shi, H.; Li, F.; Zhang, Y.; Wang, T.; Gong, W.; Zhao, X.; et al. Enhanced Energy Storage Performance in Na0.5Bi0.5TiO3-Based Relaxor Ferroelectric Ceramics via Compositional Tailoring. *Materials* **2022**, *15*, 5881. https://doi.org/10.3390/ma15175881.
30. Pattipaka, S.; Choi, H.; Lim, Y.; Park, K.-I.; Chung, K.; Hwang, G.-T. Enhanced Energy Storage Performance and Efficiency in Bi0.5(Na0.8K0.2)0.5TiO3-Bi0.2Sr0.7TiO3 Relaxor Ferroelectric Ceramics via Domain Engineering. *Materials* **2023**, *16*, 4912. https://doi.org/10.3390/ma16144912.
31. Pan, H.; Li, F.; Liu, Y.; Zhang, Q.; Wang, M.; Lan, S.; Zheng, Y.; Ma, J.; Gu, L.; Shen, Y.; et al. Ultrahigh–Energy Density Lead-Free Dielectric Films via Polymorphic Nanodomain Design. *Science (1979)* **2019**, *365*, 578–582. https://doi.org/10.1126/science.aaw8109.
32. Yang, Z.; Wang, B.; Li, Y.; Hall, D.A. Enhancement of Nonlinear Dielectric Properties in BiFeO3–BaTiO3 Ceramics by Nb-Doping. *Materials* **2022**, *15*, 2872. https://doi.org/10.3390/ma15082872.
33. Chen, Q.; Gao, T.; Lang, R.; Tan, Z.; Xing, J.; Zhu, J. Achieving Outstanding Temperature Stability in KNN-Based Lead-Free Ceramics for Energy Storage Behavior. *J Eur Ceram Soc* **2023**, *43*, 2442–2451. https://doi.org/10.1016/j.jeurceramsoc.2023.01.025.
34. Yang, Z.; Du, H.; Qu, S.; Hou, Y.; Ma, H.; Wang, J.; Wang, J.; Wei, X.; Xu, Z. Significantly Enhanced Recoverable Energy Storage Density in Potassium–Sodium Niobate-Based Lead Free Ceramics. *J Mater Chem A Mater* **2016**, *4*, 13778–13785. https://doi.org/10.1039/C6TA04107H.
35. Li, X.; Chen, X.; Sun, J.; Zhou, M.; Zhou, H. Novel Lead-Free Ceramic Capacitors with High Energy Density and Fast Discharge Performance. *Ceram Int* **2020**, *46*, 3426–3432. https://doi.org/10.1016/j.ceramint.2019.10.055.
36. Hu, D.; Pan, Z.; Tan, X.; Yang, F.; Ding, J.; Zhang, X.; Li, P.; Liu, J.; Zhai, J.; Pan, H. Optimization the Energy Density and Efficiency of BaTiO3-Based Ceramics for Capacitor Applications. *Chemical Engineering Journal* **2021**, *409*, 127375. https://doi.org/10.1016/j.cej.2020.127375.
37. Liu, B.; Wang, X.; Zhao, Q.; Li, L. Improved Energy Storage Properties of Fine-Crystalline BaTiO$_3$ Ceramics by Coating Powders with Al$_2$O$_3$ and SiO$_2$. *Journal of the American Ceramic Society* **2015**, *98*, 2641–2646. https://doi.org/10.1111/jace.13614.
38. Huang, Y.H.; Wu, Y.J.; Qiu, W.J.; Li, J.; Chen, X.M. Enhanced Energy Storage Density of Ba0.4Sr0.6TiO3–MgO Composite Prepared by Spark Plasma Sintering. *J Eur Ceram Soc* **2015**, *35*, 1469–1476. https://doi.org/10.1016/j.jeurceramsoc.2014.11.022.
39. Zhou, L.; Vilarinho, P.M.; Baptista, J.L. Dependence of the Structural and Dielectric Properties of Ba1-XSrxTiO3 Ceramic Solid Solutions on Raw Material Processing. *J Eur Ceram Soc* **1999**, *19*, 2015–2020. https://doi.org/10.1016/S0955-2219(99)00010-2.
40. Moussi, R.; Bougoffa, A.; Trabelsi, A.; Dhahri, E.; Graça, M.P.F.; Valente, M.A.; Barille, R.; Rguiti, M. Investigation of the Effect of Sr-Substitution on the Structural, Morphological, Dielectric, and Energy Storage Properties of BaTiO3-Based Perovskite Ceramics. *Inorg Chem Commun* **2022**, *137*, 109225. https://doi.org/10.1016/j.inoche.2022.109225.
41. Batllo, F.; Duverger, E.; Jules, J.-C.; Niepce, J.-C.; Jannot, B.; Maglione, M. Dielectric and E.P.R. Studies of Mn-Doped Barium Titanate. *Ferroelectrics* **1990**, *109*, 113–118. https://doi.org/10.1080/00150199008211399.

42. Morrison, F.D.; Sinclair, D.C.; West, A.R. Doping Mechanisms and Electrical Properties of La-Doped BaTiO3 Ceramics. *International Journal of Inorganic Materials* **2001**, *3*, 1205–1210. https://doi.org/10.1016/S1466-6049(01)00128-3.
43. SHAIKH, A.S.; VEST, R.W. Defect Structure and Dielectric Properties of Nd2O3-Modified BaTiO3. *Journal of the American Ceramic Society* **1986**, *69*, 689–694. https://doi.org/10.1111/j.1151-2916.1986.tb07472.x.
44. Jayanthi, S.; Kutty, T.R.N. Dielectric Properties of 3d Transition Metal Substituted BaTiO3 Ceramics Containing the Hexagonal Phase Formation. *Journal of Materials Science: Materials in Electronics* **2008**, *19*, 615–626. https://doi.org/10.1007/s10854-007-9410-6.
45. Wang, X.; Gu, M.; Yang, B.; Zhu, S.; Cao, W. Hall Effect and Dielectric Properties of Mn-Doped Barium Titanate. *Microelectron Eng* **2003**, *66*, 855–859. https://doi.org/10.1016/S0167-9317(02)01011-0.
46. Čeh, M.; Kolar, D. Solubility of Calcium Oxide in Barium Titanate. *Mater Res Bull* **1994**, *29*, 269–275. https://doi.org/10.1016/0025-5408(94)90023-X.
47. Zhao, Y.; Yang, B.; Liu, Y.; Zhou, Y.; Wu, Q.; Zhao, S. Capturing Carriers and Driving Depolarization by Defect Engineering for Dielectric Energy Storage. *ACS Appl Mater Interfaces* **2022**, *14*, 6547–6559. https://doi.org/10.1021/acsami.1c20214.
48. Liu, Q.; Liu, J.; Lu, D.; Zheng, W.; Hu, C. Structural Evolution and Dielectric Properties of Nd and Mn Co-Doped BaTiO 3 Ceramics. *J Alloys Compd* **2018**, *760*, 31–41. https://doi.org/10.1016/j.jallcom.2018.05.089.
49. Wang, Z.; Xue, D.; Zhou, Y.; Wang, N.; Ding, X.; Sun, J.; Lookman, T.; Xue, D. Enhanced Energy-Storage Density by Reversible Domain Switching in Acceptor-Doped Ferroelectrics. *Phys Rev Appl* **2021**, *15*, 034061. https://doi.org/10.1103/PhysRevApplied.15.034061.
50. Kong, S.; Kumar, N.; Checchia, S.; Cazorla, C.; Daniels, J. Defect-Driven Structural Distortions at the Surface of Relaxor Ferroelectrics. *Adv Funct Mater* **2019**, *29*, 1900344. https://doi.org/10.1002/adfm.201900344.
51. Marrocchelli, D.; Bishop, S.R.; Tuller, H.L.; Yildiz, B. Understanding Chemical Expansion in Non-Stoichiometric Oxides: Ceria and Zirconia Case Studies. *Adv Funct Mater* **2012**, *22*, 1958–1965. https://doi.org/10.1002/adfm.201102648.
52. Rini, E.G.; Paul, A.; Nasir, M.; Amin, R.; Gupta, M.K.; Mittal, R.; Sen, S. Correlation of Octahedral Distortion with Vibrational and Electronic Properties of LaFe1-Ti O3 Nanoparticles. *J Alloys Compd* **2020**, *830*, 154594. https://doi.org/10.1016/j.jallcom.2020.154594.
53. Jo, S.K.; Park, J.S.; Han, Y.H. Effects of Multi-Doping of Rare-Earth Oxides on the Microstructure and Dielectric Properties of BaTiO3. *J Alloys Compd* **2010**, *501*, 259–264. https://doi.org/10.1016/j.jallcom.2010.04.085.
54. Huang, Y.; Zhao, C.; Wu, B.; Wu, J. Multifunctional BaTiO $_3$ -Based Relaxor Ferroelectrics toward Excellent Energy Storage Performance and Electrostrictive Strain Benefiting from Crossover Region. *ACS Appl Mater Interfaces* **2020**, *12*, 23885–23895. https://doi.org/10.1021/acsami.0c03677.
55. Sun, Z.; Wang, Z.; Tian, Y.; Wang, G.; Wang, W.; Yang, M.; Wang, X.; Zhang, F.; Pu, Y. Progress, Outlook, and Challenges in Lead-Free Energy-Storage Ferroelectrics. *Adv Electron Mater* **2020**, *6*, 1900698. https://doi.org/10.1002/aelm.201900698.
56. Cha, S.H.; Han, Y.H. Effects of Mn Doping on Dielectric Properties of Mg-Doped BaTiO3. *J Appl Phys* **2006**, *100*. https://doi.org/10.1063/1.2386924.
57. Li, J.; Shen, Z.; Chen, X.; Yang, S.; Zhou, W.; Wang, M.; Wang, L.; Kou, Q.; Liu, Y.; Li, Q.; et al. Grain-Orientation-Engineered Multilayer Ceramic Capacitors for Energy Storage Applications. *Nat Mater* **2020**, *19*, 999–1005. https://doi.org/10.1038/s41563-020-0704-x.